Chemical Science

ROYAL SOCIETY OF CHEMISTRY

EDGE ARTICLE

View Article Online
View Journal | View Issue

Open Access Article. Published on 11 March 2025. Downloaded on 1/28/2026 10:07:48 AM.
This article is licensed under a Creative Commons Attribution-NonCommercial 3.0 Unported Licence.

Check for updates

Cite this: *Chem. Sci.*, 2025, **16**, 6822

All publication charges for this article have been paid for by the Royal Society of Chemistry

Received 26th January 2025
Accepted 10th March 2025

DOI: 10.1039/d5sc00713e

rsc.li/chemical-science

A triply linked propellane-nanoring hybrid serving as a good host†

Yan Chen,‡[a] Xingyu Chen,‡[b] Lin Li,‡[c] Xiangping Chen,‡[a] Jianlong Xia[b] and Lei Zhang*[a]

A novel propellane-nanoring hybrid, **TPPTI-[9]CMP**, was synthesized by triply combining [9]cyclo-*meta*-phenylene (**[9]CMP**) with triperyleno[3,3,3]propellane triimides (**TPPTI**). This structure features two **[9]CMP** subunits, which necessarily fill the voids of **TPPTI** and promote assembly of the hybrid to form a porous superstructure held together by attractive dispersion between the **[9]CMP** subunits of neighboring molecules. In the structure, three large spatial cavities are formed, which allow efficient binding of up to three C_{60} within a single hybrid. Transient absorption spectroscopy revealed that **TPPTI-[9]CMP** and C_{60} interact with each other to form a stable complex and produce long-lived triplet states. Notably, the hybrid can adsorb ethane (C_2H_6) with very excellent selectivity over ethylene (C_2H_4), leading to a highly selective C_2H_6/C_2H_4 separation.

Introduction

Triptycene is the smallest three-dimensional (3D) rigid, paddlewheel-shaped polyaromatic system and an important component of low-density materials with applications in sensors, molecular machines, and supramolecular chemistry, due to the large internal molecular free volume (IMFV) conferred by its shape-persistent geometry (Fig. 1).[1–7] In particular, the π-extended triptycenes, wherein larger ring systems are fused to the triptycene core, are conceptually interesting and practically useful, as this extension significantly increases IMFV above the bridgehead sites and between the blades.[8–19] In contrast, an alternative paddlewheel-shaped molecule, trinaphtho[3.3.3]propellane (**TNP**) (Fig. 1), though scarcely studied, has a larger π-surface and higher rigidity than triptycene, which facilitates the formation of ordered organic solids with great porosity and large surface areas.[20–23] Interest in π-extended TNPs has intensified, and recent studies have investigated their electronic and assembly properties,[24–28] diradicaloid and triradicaloid character,[29,30] gas separation,[31] and use as emitters in organic light-emitting diodes.[32,33] In 2019, we reported a new propellane, triperyleno[3,3,3]propellane triimides (**TPPTI**) (Fig. 1), which is composed of three perylene monoimide units fused on a [3,3,3]propellane.[34,35] This propellane exhibits promising characteristics, including high solubility, large π-surface, and strong electron-accepting capability. Notably, the versatile chemistry possibilities associated with **TPPTI** offer great opportunities for the development of structurally and chemically distinctive 3D compounds. However, the large flat π-blades of **TPPTI** are prone to promoting self-association by π-stacking, thereby lowering solubility and disfavoring the formation of homogeneous mixtures or cocrystals with nonplanar partners. In addition, it is reasonable to assume that the large free volume of **TPPTI**, especially around its bridgeheads, partially frustrates and inhibits packing.[36,37]

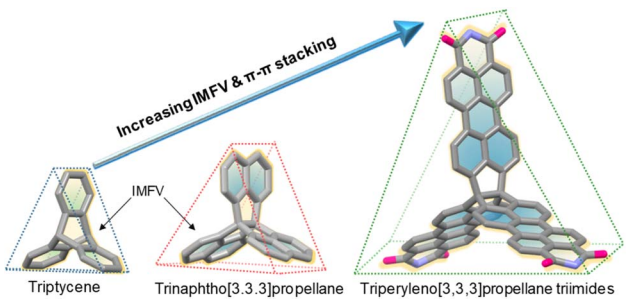

Fig. 1 Chemical structures of triptycene, trinaphtho[3.3.3]propellane, and triperyleno[3,3,3]propellane triimides with internal molecular free volume elements.

[a]Beijing Advanced Innovation Center for Soft Matter Science and Engineering, Beijing University of Chemical Technology, Beijing 100029, P. R. China. E-mail: zhl@mail.buct.edu.cn

[b]State Key Laboratory of Advanced Technology for Materials Synthesis and Processing, Center of Smart Materials and Devices, Wuhan University of Technology, Wuhan 430070, P. R. China

[c]Key Laboratory of the Ministry of Education for Advanced Catalysis Materials, College of Chemistry and Materials Science, Zhejiang Normal University, Jinhua 321004, P. R. China

† Electronic supplementary information (ESI) available. CCDC 2416459 (for **[9]CMP**), 2416457 (**TPPTI-[9]CMP**), and 2416458 (for **(C_{60})$_3$@TPPTI-[9]CMP**). For ESI and crystallographic data in CIF or other electronic format see DOI: https://doi.org/10.1039/d5sc00713e

‡ These authors contributed equally to this work.

© 2025 The Author(s). Published by the Royal Society of Chemistry

Open Access Article. Published on 11 March 2025. Downloaded on 1/28/2026 10:07:48 AM.
This article is licensed under a Creative Commons Attribution-NonCommercial 3.0 Unported Licence.

To turn **TPPTI** into effective hosts, an effective way is to make derivatives devised to block π-stacking, increase solubility, and facilitate cocrystallization. Here we report a new [*n*]cyclo-*meta*-phenylene (**[*n*]CMP**)-bearing propellane hybrid, **TPPTI-[9]CMP**, wherein the [9]cyclo-*meta*-phenylene (**[9]CMP**) subunits are triply linked to the **TPPTI** framework. It is assumed that the spatial orientation of the consecutively linked cyclophenylenes, accompanied by the conformational changes of **[*n*]CMP**, would substantially enhance excellent flexibility and porosity, which, in turn, would result in unique self-assembly or new properties.[38–40] The molecular geometry of the 3D hybrid provides three nanometer-sized cavities in the structure, as one can imagine that the **[9]CMP** subunits partially occupy the voids near the bridgeheads, promoting crystallization in a controlled orientation. This combination of a nanoring and propellane could thus open up new possibilities for supramolecular self-assembly that blend the flexibility and porosity expected for **[*n*]CMP** with enhanced binding affinities known for π-extended propellanes.

Results and discussion

A two-step synthesis of **TPPTI-[9]CMP** (Scheme 1a) started from hexabrominated **TPPTI 1**, which was prepared using the synthetic method developed by our group.[34] A six-fold Suzuki coupling of **1** with *m*-terphenyl boronic ester **2** provided **3** in 80% yield, which was converted to the desired hybrid **TPPTI-[9]CMP** in 50% yield by a six-fold intramolecular nickel-mediated Yamamoto-type homocoupling reaction. This 3D hybrid is much more soluble than **TPPTI**, and its ^{1}H NMR spectrum revealed eight nonequivalent aromatic protons, indicating the highly dynamic symmetry of the structures in solution. Additionally, the model compound **[9]CMP** was prepared by nickel-mediated cyclotrimerization of *m*-terphenyl **4**, and its molecular structure was unambiguously confirmed by X-ray crystallography (Scheme 1b).

Single crystals of **TPPTI-[9]CMP** suitable for X-ray diffraction analysis were formed from slow diffusion of methanol into chloroform solution. The X-ray structure confirmed the formation of the hybrid, which adopts a quasi-D_{3h} symmetric conformation (Fig. 2a). The three perylene monoimide units in the **TPPTI** subunit show a slight degree of twisting, presumably due to enhanced packing forces. In the structure of **TPPTI-[9]CMP**, the geometry of the **[9]CMP** subunit is different from that of parent **[9]CMP**, as measured by the C–C bond lengths and the dihedral angles between neighboring *m*-phenylene units. Interestingly, the **[9]CMP** subunit has a decrease in strain compared to parent **[9]CMP** (Fig. S11†). These observations confirmed that the configuration of **[9]CMP** is inherently deformable, which can vary in response to changes in substitution, packing, or other factors. As one structural feature, the three perylene monoimide units and two **[9]CMP** units are responsible for creating three cavities in the structure, which can efficiently obstruct π-stacking, giving the hybrid significant porosity and solubility in organic solvents even though its molecular structure is large. Thus, **TPPTI-[9]CMP** is assumed to be a good partner to cocrystallize with C_{60}. Indeed, fluorescence quenching titration of **TPPTI-[9]CMP** with C_{60} in toluene showed fluorescence quenching (Fig. S5†). The titration data were fitted to a 1 : 1 binding mode, yielding a binding constant of 7.7×10^4 M^{-1}, with no other fitting models observed. In contrast, fluorescence titration of **TPPTI** with C_{60} showed no complexation-induced quenching process (Fig. S7†). Furthermore, slow diffusion of methanol into the solution with

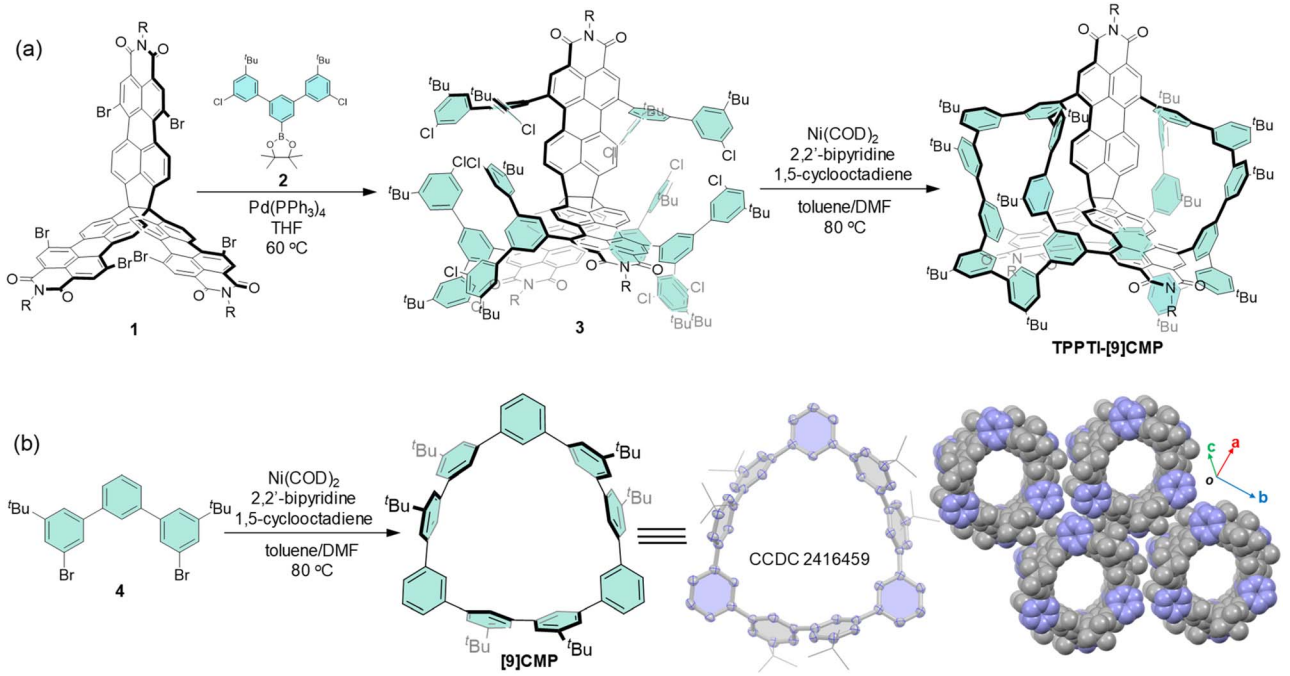

Scheme 1 (a) Synthetic steps to TPPTI-[9]CMP; (b) synthetic step to [9]CMP. Crystal structure and crystal packing of [9]CMP are shown.

Open Access Article. Published on 11 March 2025. Downloaded on 1/28/2026 10:07:48 AM.
This article is licensed under a Creative Commons Attribution-NonCommercial 3.0 Unported Licence.

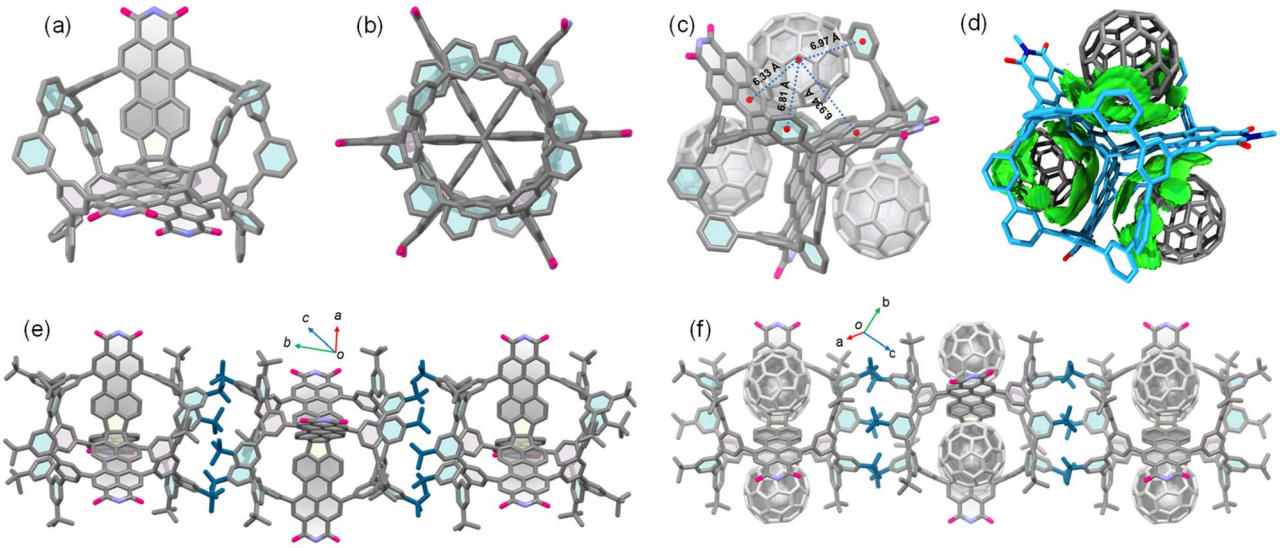

Fig. 2 (a) Crystal structure of TPPTI-[9]CMP. (b) View of the packing in TPPTI-[9]CMP, as seen down the propellane axis. (c) Crystal structure of complex $(C_{60})_3$@TPPTI-[9]CMP. (d) Optimized superstructure and the intermolecular binding iso-surface of $(C_{60})_3$@TPPTI-[9]CMP. (e and f) Crystal packing of TPPTI-[9]CMP and $(C_{60})_3$@TPPTI-[9]CMP (the substituted groups and the solvent molecules are omitted for clarity).

equimolar amounts of **TPPTI-[9]CMP** and C_{60} in toluene formed the crystals suitable for single-crystal X-ray diffraction, which revealed a 3 : 1 host–guest complex **$(C_{60})_3$@TPPTI-[9]CMP** (Fig. 2c). In the complex, each C_{60} molecule is located within one cavity, and the centroid–centroid distances between the central benzene rings in the perylene monoimide units, with C_{60} guests range from 6.33 to 6.97 Å. In addition, each C_{60} is effectively interacting with two *m*-phenylene units by C–H···π and C···C contacts. In comparison to the free host, the binding of C_{60} results in slight changes in the **[9]CMP** subunit, in which the two *m*-phenylene units slightly rotate in order to tune the cavity size to accommodate the C_{60} guest in an approximate fashion. Independent gradient model (IGM) analysis further confirmed that the strength of the binding comes from intermolecular interactions between C_{60} and perylene monoimide and **[9]CMP** units (Fig. 2d). These results suggested that the presence of the **[9]CMP** subunit appears to provide more binding sites than pristine **TPPTI**, leading to stronger binding affinity towards C_{60}. As another structural feature of **TPPTI-[9]CMP** and **$(C_{60})_3$@TPPTI-[9]CMP**, the *t*-butyl groups in **[9]CMP** subunits engage in multiple dispersion interactions to align the molecules in a columnar fashion in the direction of the propellane axis (Fig. 2b, e, and 2f), resulting in 3D porous organic frameworks in the solid state.[41,42]

The electronic structures of **[9]CMP** and **TPPTI-[9]CMP** were probed *via* density functional theory (DFT) calculations at the B3LYP/6-31G(d) level of theory. The calculated lowest unoccupied molecular orbital (LUMO) of **[9]CMP** is distributed over the whole ring, while the highest occupied molecular orbital (HOMO) is partially distributed on the ring (Fig. 3a). For **TPPTI-[9]CMP**, the HOMO is delocalized across all three perylene monoimide units and the HOMO-1 and HOMO-2 are energetically degenerate, which are delocalized on only two units. The LUMO and LUMO+1 are degenerate and delocalized over two of the three units (Fig. 3b and S9†). The HOMO-3 and HOMO-4 are degenerate and partially delocalized over the **[9]CMP** subunits; however, no significant π-electron orbital mixing between the **TPPTI** and **[9]CMP** subunits is observed (Fig S10†). **TPPTI-[9]CMP** and **TPPTI** exhibit a very similar absorption profile in the wavelength range between approximately 480 to 640 nm, although slightly red-shifted (∼13 nm), as the main transitions are localized on the **TPPTI** subunit (Fig. 3c). Additionally, **TPPTI-[9]CMP** possesses one major absorption at 266 nm, which correlates with the **[9]CMP** subunit, corresponding to the HOMO-2 and HOMO-3 to LUMO+3 and LUMO+4 transitions (Table S2†). As expected, both **TPPTI-[9]CMP** and **TPPTI** have similar fluorescence profiles, fluorescence quantum yields (87% *vs.* 85%), and lifetimes (4.4 ns *vs.* 3.8 ns) (Fig. 3c and S12†). In comparison, note that **[9]CMP** has a poorer fluorescence

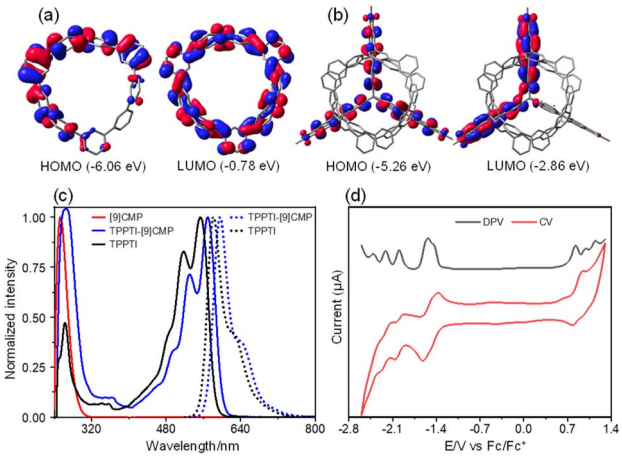

Fig. 3 (a and b) Calculated molecular orbitals of [9]CMP and TPPTI-[9]CMP. (c) UV-vis spectra (solid line) of [9]CMP, TPPTI, and TPPTI-[9]CMP and emission spectra (dashed line) of TPPTI, and TPPTI-[9]CMP. (d) Cyclic voltammogram and differential pulse voltammogram of TPPTI-[9]CMP.

 © 2025 The Author(s). Published by the Royal Society of Chemistry

Open Access Article. Published on 11 March 2025. Downloaded on 1/28/2026 10:07:48 AM.
This article is licensed under a Creative Commons Attribution-NonCommercial 3.0 Unported Licence.

quantum yield of 10% and a shorter lifetime of 1.0 ns. This suggests that the **TPPTI** subunit is dominating the excited state processes for the hybrid.

Cyclic voltammetry (CV) and differential pulse voltammetry (DPV) studies were performed in dichloromethane, and the redox potentials were determined relative to ferrocene/ferrocenium (Fc/Fc^+). Compared to perylene monoimide (PMI) exhibiting two reversible one-electron reduction waves and a reversible one-electron oxidation wave,[34] **TPPTI-[9]CMP** undergoes a six-electron reversible reduction process, which involves a reversible one-electron wave at −1.44 V, corresponding to the formation of a singly reduced PMI radical anion, two reversible one-electron waves at −1.53 V, corresponding to the formation of two singly reduced PMI radical anions, three reversible one-electron waves at −1.99, −2.21, and −2.41 V, corresponding to the formation of three singly reduced PMI dianions, and a reversible one-electron wave at −2.18 V, corresponding to the formation of a singly reduced PMI dianion. In addition, the CV of **TPPTI-[9]CMP** shows three one-electron oxidation waves at 0.84, 0.98, and 1.15 V, corresponding to the formation of three singly oxidized PMI radical cations.

Furthermore, the excited-state evolution process for **TPPTI-[9]CMP** and **$(C_{60})_3$@TPPTI-[9]CMP** was investigated by femtosecond and nanosecond transient absorption spectroscopy (fs- and ns-TA). Upon excitation at 520 nm, **TPPTI-[9]CMP** in chloroform initially shows a broad excited state absorption (ESA) band from 600 to 750 nm and ground-state bleaching (GSB) bands at 528 and 568 nm (Fig. 4a–c). Within the ultrafast timescale (∼1 ps), the ESA band is split into two bands at 620 nm and 680 nm and the overall spectral shape does not change throughout the test window. Specifically, the intensity and dynamics of the sub-peak at ∼610 nm are controlled by solvent polarity (Fig. S13†). We attributed the ESA band at ∼610 nm to the CT state character of **TPPTI-[9]CMP**, which originates from the vibrational relaxation process of the photoinduced excited states. We further clarify the assignment for the CT state with normalized comparison of decay profiles and global analysis for fs-TA in toluene and chloroform (Fig. S14 and S15†). In addition, the spectral shapes in ns-TA are in accordance with those in fs-TA, which are assigned to the singlet state with CT character with a lifetime of 3–4 ns (Fig. S17 and S18†).

In the case of **$(C_{60})_3$@TPPTI-[9]CMP**, the broad ESA band from 600 nm to 750 nm and GSB band at 570 nm initially occur upon excitation at 530 nm (Fig. 4d–f). Subsequently, both ESA and GSB signals decay rapidly within the instrument resolution time, and ESA converts into two bands with CT character, indicating a fast CS process. Then a new ESA band at 500 nm appears, and the GSB band red-shifts to 580 nm. The growth and decay processes of new species are out of the test window. The lifetime of this long-lived state for **$(C_{60})_3$@TPPTI-[9]CMP** can reach up to 300–400 μs (Fig. S19 and S20†), which is significantly prolonged relative to **TPPTI-[9]CMP**. The sensitization experiment revealed that the spectra of the sensitized triplet state for **TPPTI-[9]CMP** is in good coincidence with that of long-lived species, indicating that the triplet state is mainly located on **TPPTI-[9]CMP** (Fig. S21†).

On the basis of the above discussion, we inferred that **TPPTI-[9]CMP** might relax into the charge transfer state upon excitation (Fig. S22†), which decays to the ground state through a radiative pathway, leading to near-quantitative fluorescence quantum yield. In contrast, the CS process might be accelerated in **$(C_{60})_3$@TPPTI-[9]CMP**, which subsequently undergoes a charge recombination process to produce triplet states with the mechanism of radical-pair intersystem crossing (RP-ISC) (Fig. S22†).[43,44] The long-lived triplets are proved to be located on **TPPTI-[9]CMP** and decay with a lifetime of hundreds of microseconds. The charge separation and RP-ISC process compete with the fluorescence process, resulting in severe fluorescence quenching in **$(C_{60})_3$@TPPTI-[9]CMP**.

The intrinsic porosity and large π-framework in **TPPTI-[9]CMP** motivate us to further investigate its potential for ethane (C_2H_6)/ethylene (C_2H_4) separation.[45,46] The packing of the hybrids in the solid state is determined by intermolecular C–

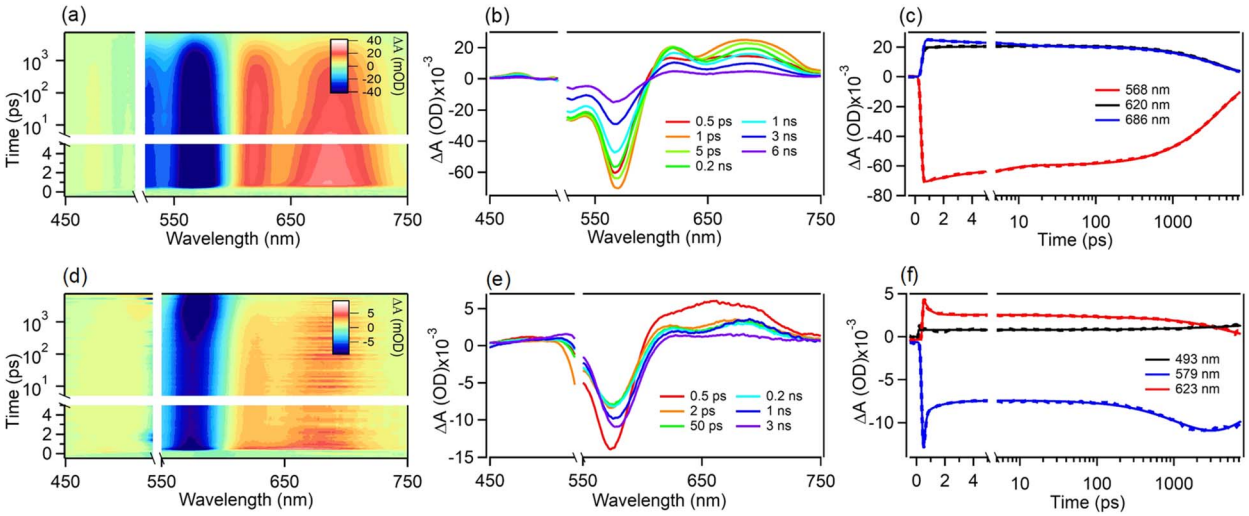

Fig. 4 2D contour maps, transient absorption spectra and decay profiles of TPPTI-[9]CMP (a–c) and $(C_{60})_3$@TPPTI-[9]CMP (d–f) in dilute chloroform solution with excitation at 520 nm and 530 nm, respectively.

Open Access Article. Published on 11 March 2025. Downloaded on 1/28/2026 10:07:48 AM.
This article is licensed under a Creative Commons Attribution-NonCommercial 3.0 Unported Licence.

H···π and C–H···O interactions, resulting in a 3D porous network with honeycomb-shaped channels. The porous network contains void spaces, with pore sizes of 11.7 Å × 5.9 Å (Fig. S23†). The nitrogen sorption isotherm measured at 77 K revealed that **TPPTI-[9]CMP** has a Brunauer–Emmett–Teller (BET) surface area of 165 m^2 g^{-1} (Fig. S24†). The single-component adsorption experiments were performed on C_2H_6 and C_2H_4 at different temperatures (273, 283, and 298 K) using activated **TPPTI-[9]CMP** (Fig. S25†), which revealed that the adsorption of C_2H_6 consistently exceeds that of C_2H_4 across the entire pressure range at different temperatures. At 298 K and 1 bar, the adsorbed amount of C_2H_6 for **TPPTI-[9]CMP** reached approximately 32.4 cm^3 g^{-1}, which is significantly higher than that of C_2H_4 (16.5 cm^3 g^{-1}) (Fig. 5a). The isosteric heats of adsorption (Q_{st}) for C_2H_6 were calculated to be between 17.2 and 21.4 kJ mol^{-1} using the virial equation (Fig. 5c and Table S5†), which are higher than those of C_2H_4 (11.6 to 16.3 kJ mol^{-1}), indicating a stronger gas bonding affinity for C_2H_6.

These results are further supported by dispersion-corrected density-functional theory calculations (DFT-D), which predicted the static binding energies for C_2H_6 and C_2H_4 to be approximately 32.7 and 25.4 kJ mol^{-1}, respectively. The increased binding energy can primarily be attributed to the enhanced steric complementarity between the C_2H_6 molecule and the cavity of **TPPTI-[9]CMP** when compared to C_2H_4.[47] This is likely due to more efficient C–H···π interactions and hydrogen bonding for C_2H_6 than for C_2H_4 (Fig. S28†). Our calculations also indicated that the C_2H_6 molecules preferentially locate in the cavity and the C–H···N hydrogen bonding might play a dominant role in C_2H_6-selectivity (Fig. S28†). In addition, the selectivity of **TPPTI-[9]CMP** towards C_2H_6 and C_2H_4 is estimated to be 2.46 by the ideal solution theory (IAST, Fig. 5b). This value surpasses those reported for other high-performance C_2H_6-selective organic adsorbents at 298 K and 1 bar (Fig. 5d and Table S4†).[48] A breakthrough experiment was finally conducted in a fixed-bed column using a binary gas mixture of C_2H_6/C_2H_4 (50/50, v/v) at 298 K (Fig. S26†). C_2H_4 first breaks through the packed column at 40 seconds, while C_2H_6 begins to break through after 258 seconds. During this interval, polymer-grade purity (>99.95%) C_2H_4 can be collected. Overall, these results highlight the potential of the hybrid for efficient gas separation.

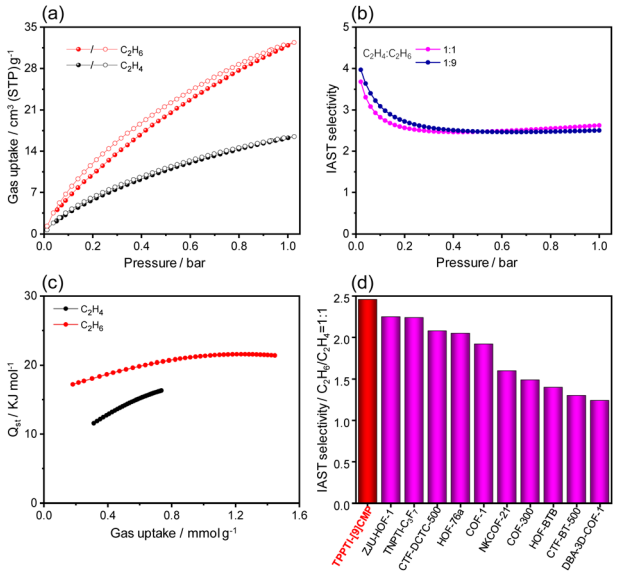

Fig. 5 (a) Single component adsorption isotherms of C_2H_6 and C_2H_4 at 298 K. (b) Q_{st} curves for TPPTI-[9]CMP. (c) IAST selectivity of C_2H_6/C_2H_4 (1 : 1, v/v, without gas carrier) mixtures at 298 K. (d) Comparison of IAST selectivities of the C_2H_6/C_2H_4 (1 : 1, v/v) mixture for TPPTI-[9]CMP with previously reported pure organic C_2H_6-selective adsorbents at 298 K and 1 bar.

Conclusions

In conclusion, we have designed and synthesized a nanoring-propellane hybrid, in which two **[9]CMP** units are triply linked to the **TPPTI** framework. A comparison between **TPPTI** and the hybrid reveals that the presence of the **[9]CMP** unit plays an important role in the crystallization and assembly of the hybrid. Of particular interest is that crystallizing this hybrid produces a superstructure with significant porosities for guest inclusion. We believe that the development of this unique hybrid with the nanoring unit and propellane framework will allow its potential usage for binding a variety of guest species, fullerene extraction, and gas separation, overcoming some of the crystallinity and assembly limitations that have previously hindered the development of this field.

Data availability

Detailed synthesis and characterization of the related compounds, crystal data for **[9]CMP**, **TPPTI-[9]CMP**, and **$(C_{60})_3$@TPPTI-[9]CMP**, along with ^{1}H NMR, ^{13}C NMR, high-resolution mass spectra (HRMS) of the related compounds, CV, UV, and PL measurements, PL titration, transient absorption measurements, gas adsorption tests, and theoretical calculation details, are available in the ESI.†

Author contributions

L. Z and J. Xia conceived and designed the project. Y. C and X. C synthesized and characterized the compounds. X. C performed transient absorption measurements. L. L performed gas adsorption measurements. All authors discussed the results and contributed to the manuscript preparation.

Conflicts of interest

There are no conflicts to declare.

Acknowledgements

This work was financially supported by the National Key Research and Development Program of China (2022YFC2106100) and the National Natural Science Foundation of China (NSFC) (22175013).

 © 2025 The Author(s). Published by the Royal Society of Chemistry

Open Access Article. Published on 11 March 2025. Downloaded on 1/28/2026 10:07:48 AM.
This article is licensed under a Creative Commons Attribution-NonCommercial 3.0 Unported Licence.

Notes and references

1 P. D. Bartlett, M. J. Ryan and S. G. Cohen, *J. Am. Chem. Soc.*, 1942, **64**, 2649.
2 Y. Jiang and C.-F. Chen, *Eur. J. Org Chem.*, 2011, **32**, 6377.
3 T. M. Swager, *Acc. Chem. Res.*, 2008, **41**, 1181.
4 J.-R. Mistry, S. Montanaro and I. A. Wright, *Mater. Adv.*, 2023, **4**, 787.
5 Y. Han, Z. Meng, Y.-X. Ma and C.-F. Chen, *Acc. Chem. Res.*, 2014, **47**, 2026.
6 J. H. Chong and M. J. MacLachlan, *Chem. Soc. Rev.*, 2009, **38**, 3301.
7 C.-F. Chen and Y. Han, *Acc. Chem. Res.*, 2018, **51**, 2093.
8 Y. Duan, G. Zhang, X. Liu, F. Shi, T. Wang, H. Yan, H. Xu and L. Zhang, *J. Org. Chem.*, 2022, **87**, 8841.
9 B. Kohl, F. Rominger and M. Mastalerz, *Angew. Chem., Int. Ed.*, 2015, **54**, 6051.
10 B. Kohl, F. Rominger and M. Mastalerz, *Chem. Eur J.*, 2015, **21**, 17308.
11 S. Montanaro, D. G. Congrave, M. K. Etherington and I. A. Wright, *J. Mater. Chem. C*, 2019, **7**, 12886.
12 D. Reinhard, F. Rominger and M. Mastalerz, *J. Org. Chem.*, 2015, **80**, 9342.
13 B. Kohl, F. Rominger and M. Mastalerz, *Org. Lett.*, 2014, **16**, 704.
14 K. Baumgärtner, M. Hoffmann, F. Rominger, S. M. Elbert, A. Dreuw and M. Mastalerz, *J. Org. Chem.*, 2020, **85**, 15256.
15 Z. Liu, W. Song, S. Yang, C. Yuan, Z. Liu, H.-L. Zhang and X. Shao, *Chem.–Eur. J.*, 2022, **28**, e202200306.
16 S. R. Peurifoy, E. Castro, F. Liu, X. Y. Zhu, F. Ng, S. Jockusch, M. L. Steigerwald, L. Echegoyen, C. Nuckolls and T. J. Sisto, *J. Am. Chem. Soc.*, 2018, **140**, 9341.
17 P. Kissel, D. J. Murray, W. J. Wulftange, V. J. Catalano and B. T. King, *Nat. Chem.*, 2014, **6**, 774.
18 D. J. Murray, D. D. Patterson, P. Payamyar, R. Bhola, W. Song, M. Lackinger, A. D. Schlüter and B. T. King, *J. Am. Chem. Soc.*, 2015, **137**, 3450.
19 M. K. Amin, C. Ye, S. Pang, Y. Liu, D. Taylor, G. S. Nichol and N. B. McKeown, *Chem. Sci.*, 2024, **15**, 14968.
20 G. Dyker, J. Körning, P. G. Jones and P. Bubenitschek, *Angew Chem. Int. Ed. Engl.*, 1993, **32**, 1733.
21 G. Dyker, J. Körning, F. Nerenz, P. Siemsen, S. Sostmann and A. Wiegand, *Pure Appl. Chem.*, 1996, **68**, 323.
22 G. Dyker, T. Kerl, J. Körning, P. Bubenitschek and P. G. Jones, *Tetrahedron*, 2000, **56**, 8665.
23 T. Kubo, S. Miyazaki, T. Kodama, M. Aoba, Y. Hirao and H. Kurata, *Chem. Commun.*, 2015, **51**, 3801.
24 T. Kodama, S. Miyazaki and T. Kubo, *ChemPlusChem*, 2019, **84**, 599.
25 K. Kato, S. Tanaka, N. Seto, K. Wada, M. Gon, S. Fa, S. Ohtani, K. Tanaka and T. Ogoshi, *Chem. Commun.*, 2023, **59**, 7080.
26 T. Kodama, Y. Hirao, T. Nishiuchi and T. Kubo, *ChemPlusChem*, 2017, **82**, 1006.
27 S. Kawai, O. Krejčí, T. Nishiuchi, K. Sahara, T. Kodama, R. Pawlak, E. Meyer, T. Kubo and A. S. Foster, *Sci. Adv.*, 2020, **6**, eaay8913.
28 K. Kato, Y. Uchida, T. Kaneda, T. Tachibana, S. Ohtani and T. Ogoshi, *Chem. Asian J.*, 2024, **19**, e202400080.
29 T. Kodama, M. Aoba, Y. Hirao, S. M. Rivero, J. Casado and T. Kubo, *Angew. Chem., Int. Ed.*, 2022, **61**, e202200688.
30 T. Kodama, Y. Hirao and T. Kubo, *Precis. Chem.*, 2023, **1**, 183.
31 Y. Chen, Y. Zhao, Y. Zhao, X. Chen, X. Liu, L. Li, D. Cao, S. Wang and L. Zhang, *Angew. Chem., Int. Ed.*, 2024, **63**, e202401706.
32 L. Hua, Y. Liu, B. Liu, Z. Zhao, L. Zhang, S. Yan and Z. Ren, *Nat. Commun.*, 2022, **13**, 7828.
33 Z. Zhao, S. Yan and Z. Ren, *Acc. Chem. Res.*, 2023, **56**, 1942.
34 L. Lv, J. Robert, C. Xiao, Z. Jia, W. Jiang, G. Zhang, C. Risko and L. Zhang, *Chem. Sci.*, 2019, **10**, 4951.
35 L. Lv, W. Sun, Z. Jia, G. Zhang, F. Wang, Z. Tan and L. Zhang, *Mater. Chem. Front.*, 2020, **4**, 3539.
36 L. J. Abbott, N. B. McKeown and C. M. Colina, *J. Mater. Chem. A*, 2013, **1**, 11950.
37 C. L. Hilton, C. R. Jamison, H. K. Zane and B. T. King, *J. Org. Chem.*, 2009, **74**, 405.
38 C. Zhou, R. Li, Y. Chen, X. Liu, H. Zhao, X.-Q. Yang, Z. Ren, D. Wang, Z. Wang and L. Zhang, *CCS Chem.*, 2024, **6**, 2427.
39 K. Ikemoto, R. Kobayashi, S. Sato and H. Isobe, *Angew. Chem., Int. Ed.*, 2017, **56**, 6511.
40 K. Ikemoto and H. Isobe, *Bull. Chem. Soc. Jpn.*, 2021, **94**, 281.
41 B. Kohl, M. V. Bohnwagner, F. Rominger, H. Wadepohl, A. Dreuw and M. Mastalerz, *Chem. Eur J.*, 2016, **22**, 646.
42 L. Ueberricke and M. Mastalerz, *Chem. Rec.*, 2021, **21**, 558.
43 D. Sasikumar, A. T. John, J. Sunny and M. Hariharan, *Chem. Soc. Rev.*, 2020, **49**, 6122.
44 X. Wang, Y. Song, G. Pan, W. Han, B. Wang, L. Cui, H. Ma, Z. An, Z. Xie, B. Xu and W. Tian, *Chem. Sci.*, 2020, **11**, 10921.
45 D. S. Sholl and R. Lively, *Nature*, 2016, **532**, 435.
46 L. Li, R.-B. Lin, R. P. Krishna, H. Li, S. Xiang, H. Wu, J. Li, W. Zhou and B. Chen, *Science*, 2018, **362**, 443.
47 K. Su, W. Wang, S. Du, C. Ji and D. Yuan, *Nat. Commun.*, 2021, **12**, 3703.
48 X. Zhang, J.-X. Wang, L. Li, J. Pei, R. Krishna, H. Wu, W. Zhou, G. Qian, B. Chen and B. Li, *Angew. Chem., Int. Ed.*, 2021, **60**, 10304.

© 2025 The Author(s). Published by the Royal Society of Chemistry